

# Spectral evidence of an accretion disk in wind-fed X-ray pulsar Vela X-1 during an unusual spin-up period

Zhenxuan Liao<sup>1,2</sup>, Jiren Liu<sup>1\*</sup>, Xueying Zheng<sup>1,2</sup>, and Lijun Gou<sup>1,2</sup>

<sup>1</sup>Key Laboratory for Computational Astrophysics, National Astronomical Observatory, Chinese Academy of Sciences, Datun Road 20A, Beijing 100012, People's Republic of China

<sup>2</sup>School of Astronomy and Space Science, University of Chinese Academy of Sciences, Beijing 100049, People's Republic of China

Accepted XXX. Received YYY; in original form ZZZ

## ABSTRACT

In classical supergiant X-ray binaries (SgXBs), the Bondi-Hoyle-Lyttleton wind accretion was usually assumed, and the angular momentum transport to the accretors is inefficient. The observed spin-up/spin-down behavior of the neutron star in SgXBs is not well understood. In this paper, we report an extended low state of Vela X-1 (at orbital phases 0.16–0.2), lasting for at least 30 ks, observed with *Chandra* during the onset of an unusual spin-up period. During this low state, the continuum fluxes dropped by a factor of 10 compared to the preceding flare period, and the continuum pulsation almost disappeared. Meanwhile, the Fe K $\alpha$  fluxes of the low state were similar to the preceding flare period, leading to an Fe K $\alpha$  equivalent width (EW) of 0.6 keV, as high as the Fe K $\alpha$  EW during the eclipse phase of Vela X-1. Both the pulsation cessation and the high Fe K $\alpha$  EW indicate an axisymmetric structure with a column density larger than  $10^{24}$  cm<sup>-2</sup> on a spatial scale of the accretion radius of Vela X-1. These phenomena are consistent with the existence of an accretion disk that leads to the following spin-up of Vela X-1. It indicates that disk accretion, although not always, does occur in classical wind-fed SgXBs.

**Key words:** Pulsars: individual: Vela X-1 – X-rays: binaries

## 1 INTRODUCTION

In supergiant X-ray binaries (SgXBs), the X-ray radiation is powered by accretion of massive stellar wind to the compact neutron star or black hole. The accretion processes involve many physical factors, such as the clumpy wind, the strong magnetic field of the neutron star, the dynamical interaction, and the photoionization, all of which make the accretion processes of wind-fed SgXBs not fully understood (for a recent review, see [Martínez-Núñez et al. 2017](#)). In classical SgXBs, like Vela X-1, the Bondi-Hoyle-Lyttleton wind accretion was usually assumed ([Davidson & Ostriker 1973](#)), and the angular momentum transport to the neutron star is inefficient. Their pulse periods, however, show alternative spin-up and spin-down, superimposed on a longer trend of either spin-up or spin-down (e.g. [Bildsten et al. 1997](#)). The pulse frequency variations of Vela X-1 were explained as a random walk in pulse frequency ([Deeter et al. 1989](#)). The angular momentum transport in wind-fed SgXBs was first discussed by [Shapiro & Lightman \(1976\)](#) and [Wang \(1981\)](#), and recently by [Karino et al. \(2019\)](#), among others. They

found that when the binary orbit is tight and the stellar wind is slow, the spatial gradient of density and velocity could lead to the formation of a disk.

The formation of a disk-like structure in Vela X-1 was recently evaluated with hydrodynamic simulations by [El Mellah et al. \(2019b\)](#). They found that when the wind velocity at the position of the neutron star is comparable to the orbital velocity, the wind is seriously beamed, and a disk-like structure is formed in the shocked region for a configuration of a heavy neutron star. Because Vela X-1 is an eclipsing system and the wind-captured disk is expected to form within the orbital plane, [El Mellah et al. \(2019b\)](#) pointed out that the disk would intercept the line-of-sight and might significantly contribute to the observed absorption column density.

Discovered in the early years of X-ray astronomy ([Chodil et al. 1967](#)), Vela X-1 is one of the best studied SgXBs (for a recent review, see [Kretschmar et al. 2019](#)). It has a pulse period of 283 s ([McClintock et al. 1976](#)) and a magnetic field around  $2.6 \times 10^{12}$  G (e.g. [Kretschmar et al. 1996](#)). The optical companion, HD 77581, is a B0.5 Ib supergiant, with a radius of  $30.0 R_{\odot}$  and a mass of  $23.5 M_{\odot}$  ([van Kerkwijk et al. 1995](#)). The binary system has an orbital period of 8.9644 days ([Falanga et al. 2015](#)), a tight orbital

\* E-mail: jirenliu@nao.cas.cn

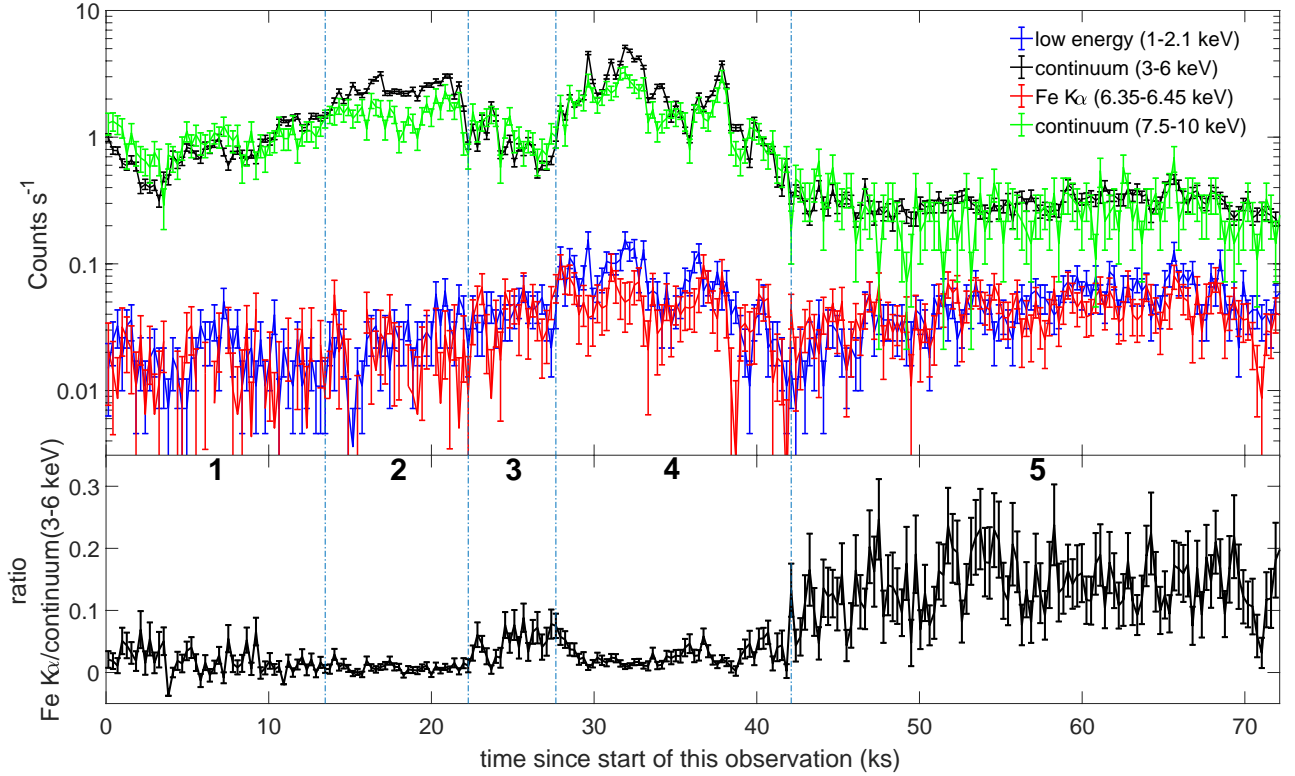


**Figure 2.** Light curves of the low-energy band (1–2.1 keV), the Fe  $K\alpha$  line (6.35–6.45 keV), and the continuum within 3–6 keV and 7.5–10 keV band of Vela X-1 from *Chandra* observation (top panel), along with the ratio of Fe  $K\alpha$  to continuum within 3–6 keV (bottom panel). The time resolution is 283.6 s. A baseline continuum (40% of the count rate in the 6–6.2 keV band) has been subtracted from the Fe  $K\alpha$  fluxes. For clarity, the rates of 7.5–10 keV continuum are multiplied by a factor of 10. The individual segments analyzed later are marked as numbers of 1–5. Error bars indicate  $1\sigma$  uncertainty.

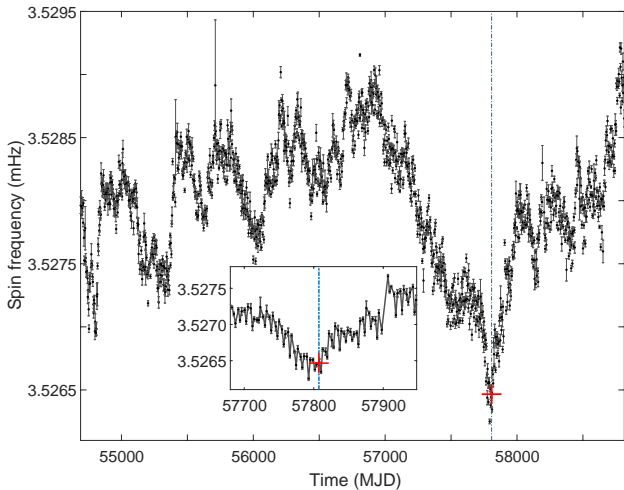


**Figure 1.** The pulse frequency history of Vela X-1 monitored with *Fermi*/GBM. Over-plotted red cross marks the *Chandra* observation taken at the onset of the spin-up event.

separation of  $53.4 R_{\odot}$  (van Kerkwijk et al. 1995), a low eccentricity  $e \approx 0.09$  (e.g. Boynton et al. 1986), and a high

inclination ( $i > 73^{\circ}$ , Joss & Rappaport 1984). The distance to Vela X-1 was estimated to be  $1.9 \pm 0.2$  kpc (Sadakane et al. 1985).

In this paper we report evidences of an accretion disk in Vela X-1 observed by *Chandra* during the onset of an unusual spin-up period. This *Chandra* observation of Vela X-1 showed an extended low state, lasting for at least 30 ks, until the end of the observation. During this low state, the continuum fluxes reduced by an order of magnitude, and their pulsations almost disappeared, while the Fe  $K\alpha$  fluxes were similar to those preceding the low state, leading to an Fe  $K\alpha$  equivalent width (EW) of 0.6 keV. Such a high Fe  $K\alpha$  EW is only observed to appear during the eclipse phase of Vela X-1 previously. If not specified, the quoted errors are for 90% confidence level.

## 2 OBSERVATIONS

Thanks to the Burst and Transient Source Experiment (BATSE) on the *Compton* gamma ray observatory and Gamma-ray Burst Monitor (GBM, Jenke & Wilson-Hodge 2017) on the *Fermi* gamma ray telescope, the spin history of X-ray pulsars can be continuously monitored. The spin history of Vela X-1 monitored by *Fermi*/GBM is presented in Fig. 1. Rapid changes of spin-up and spin-down on tens of days are clearly seen. A spin-up event around MJD 57800

(Feb. 16th, 2017) seems unusual, in the sense that it occurred around the lowest spin frequency monitored by GBM, with a sharp transition from spin-down to spin-up, and it seems to have a longest continuous spin-up period ( $\sim 200$  days), although showing some flat spin periods in between. Other spin-up periods last only for about 50 days. This spin frequency ( $\sim 3.5265$  mHz) is also the lowest one compared with those monitored by BATSE and other early pointing observations<sup>1</sup>.

Vela X-1 was happened to be observed by *Chandra* High Energy Transmission Grating (HETG, Canizares et al. 2005) at the onset of this unusual spin-up period (ObsID 19953, PI Canizares, on Feb. 22nd, 2017, MJD 57806.98). The observation was taken at the orbital phase  $\phi = 0.107 - 0.203$ , while the eclipse phase of Vela X-1 is  $\phi_{\text{ecl}} = 0.9204 - 0.0899$  (according to the ephemeris of Falanga et al. 2015, their Table 3). The phase zero is defined as the time of mid-eclipse,  $T_{\text{ecl}}$ , which is 0.2 days later than the time of mean longitude,  $T_{\pi/2}$ . The exposure time was 70 ks. We downloaded the data from *Chandra* archive and reprocessed it with TG-CAT script (Huenemoerder et al. 2011) following the standard procedure. A narrow spatial mask is used to improve the fluxes above 7 keV. The barycentric correction is applied with AXBARY tool within CIAO software and the binary effect is corrected with the program *binaryCor* in Reemis ISIScripts<sup>2</sup>. The time periodicity was analysed with *sitar\_epfold\_rate* and *sitar\_pfold\_rate* tools within the SITAR package<sup>3</sup>. We only used the first order HEG data, because of its better spectral resolution and larger effective area in the Fe K $\alpha$  band than higher order data.

### 3 TIMING RESULTS

The extracted light curves of the low-energy band (1–2.1 keV), the Fe K $\alpha$  line (6.35–6.45 keV), and the continua within 3–6 keV and 7.5–10 keV are presented in Fig. 2. A baseline continuum, estimated as 40% of the count rate in the 6.0–6.2 keV band, is subtracted from the Fe K $\alpha$  fluxes. The coefficient of 40% is estimated from the flux ratio between 6.35–6.45 keV and 6.0–6.2 keV from an absorbed powerlaw model fitted to the spectrum of the observation. All light curves are binned to 283.6 s. The best pulse period estimated with the EFSEARCH program in FTOOLS from the first 40 ks of the observation is 283.57 s, consistent with the spin frequency measured with *Fermi*/GBM (Fig. 1). As can be seen from Fig. 2, the continua within 3–6 keV and 7.5–10 keV show similar trends, while the trend of the low-energy band (1–2.1 keV) is similar to that of the Fe K $\alpha$  line. The continua show two flares around 20 ks and 35 ks, and then they enter an extended low state from 42 ks, keeping quiescent until the end of the observation. On the other hand, the Fe K $\alpha$  line reaches a high level during the flare around 35 ks, and then it drops a little and back to a high level later. The flux ratios between the Fe K $\alpha$  and the continuum within 3–6 keV are plotted in the bottom panel of Fig. 2. The ratios with respect to the continuum within 7.5–10 keV are similar and not presented. The average Fe K $\alpha$ /3–6 keV ratios are

0.02 and 0.14, during the first 42 ks and thereafter, respectively. Based on the flux levels of different bands, we divide the observation into five segments: 0–13.5 ks (1), 13.5–22.3 ks (2), 22.3–27.7 ks (3), 27.7–42.1 ks (4), and 42.1–72.2 ks (5).

For each segment, we search for periodicity in the continua within 3–6 keV and 7.5–10 keV, the low-energy band (1–2.1 keV), and the Fe K $\alpha$  line with the epoch folding method for light curves binned in 10 s. The trial periods are between 100 s and 400 s, with a step of 0.1 s and 20 phase bins. The significances of periodicity (L-statistics; Leahy et al. 1983; Davies 1990) of the trial periods are plotted in Fig. 3. As can be seen, both the continua within 3–6 keV and 7.5–10 keV of Seg. 1–4 show clear pulsations with a period  $\sim 283.6$  s, while their periodicity is almost disappeared in Seg. 5. On the other hand, as expected, the low-energy band and the Fe K $\alpha$  line show no apparent periodicity in all five segments.

To calculate the pulse profiles of the continuum, we fold the 3–6 keV light curves of all five segments with the period of 283.57 s with 20 phase bins. The resulting pulse profiles are plotted in the left panel of Fig. 4, and for clarity, the pulse profile of Seg. 5 is multiplied by a factor of 12. The profiles of Seg. 1–4 show regular five-peaked behavior (Raubenheimer 1990), while the profile of Seg. 5 is close to flat. The pulse profiles of the continuum within 7.5–10 keV are plotted in the right panel of Fig. 4. They show a similar behavior as the continuum within 3–6 keV, but with larger uncertainties due to lower counts. For each segment, we calculate the pulsed fraction of the continuum, which is defined as  $f = \frac{\max(p) - \min(p)}{\max(p) + \min(p)}$ , where  $p$  represents the value of pulse profile. For Seg. 1–5, the pulsed fractions of the continuum within 3–6 keV are 0.42, 0.46, 0.53, 0.48, and 0.11, respectively, while the pulsed fractions within 7.5–10 keV are 0.39, 0.49, 0.57, 0.36, and 0.26, respectively.

### 4 SPECTRAL RESULTS

The extracted spectra of all five segments are plotted in Fig. 5. They are binned with a piecewise minimum signal-to-ratio (S/N) of 5, 11, and 8 for energy ranges of 1–3, 3–6, and 6–10 keV, respectively. As can be seen, the continua of the two flares in Seg. 2 and Seg. 4 are clearly higher than other segments. The continuum drops significantly for Seg. 5, while the continua of Seg. 1 and 3 are in between. Meanwhile, the Fe K $\alpha$  line is relatively low for the first two segments and starts to increase from Seg. 3. The drop of the continuum of Seg. 5 makes its Fe K $\alpha$  line very prominent. There is a redward wing of the Fe K $\alpha$  line of Seg. 5, which is likely the Compton shoulder of the Fe K $\alpha$  line. The Fe K $\beta$  line and highly-ionized Fe XXV and Fe XXVI lines are also clearly seen in the spectrum of Seg. 5. The spectrum of Seg. 4 also shows similar highly-ionized Fe lines, but with a lower contrast due to a higher continuum level. Similar to the Fe K $\alpha$  line, the low-energy lines (1–2.1 keV) of the low state of Seg. 5 are as bright as those of Seg. 4.

To quantify the spectral differences of different segments, we fit the spectra with a phenomenological model, consisting of an absorbed powerlaw and a Gaussian line (representing the Fe K $\alpha$  line). The centroid of Fe K $\alpha$  line has been fixed to 6.3995 keV, which is the weighted

<sup>1</sup> <https://gammaray.nsstc.nasa.gov/batse/pulsar>

<sup>2</sup> <http://www.sternwarte.uni-erlangen.de/isis>

<sup>3</sup> <http://space.mit.edu/cxc/analysis/SITAR/distrib.html>

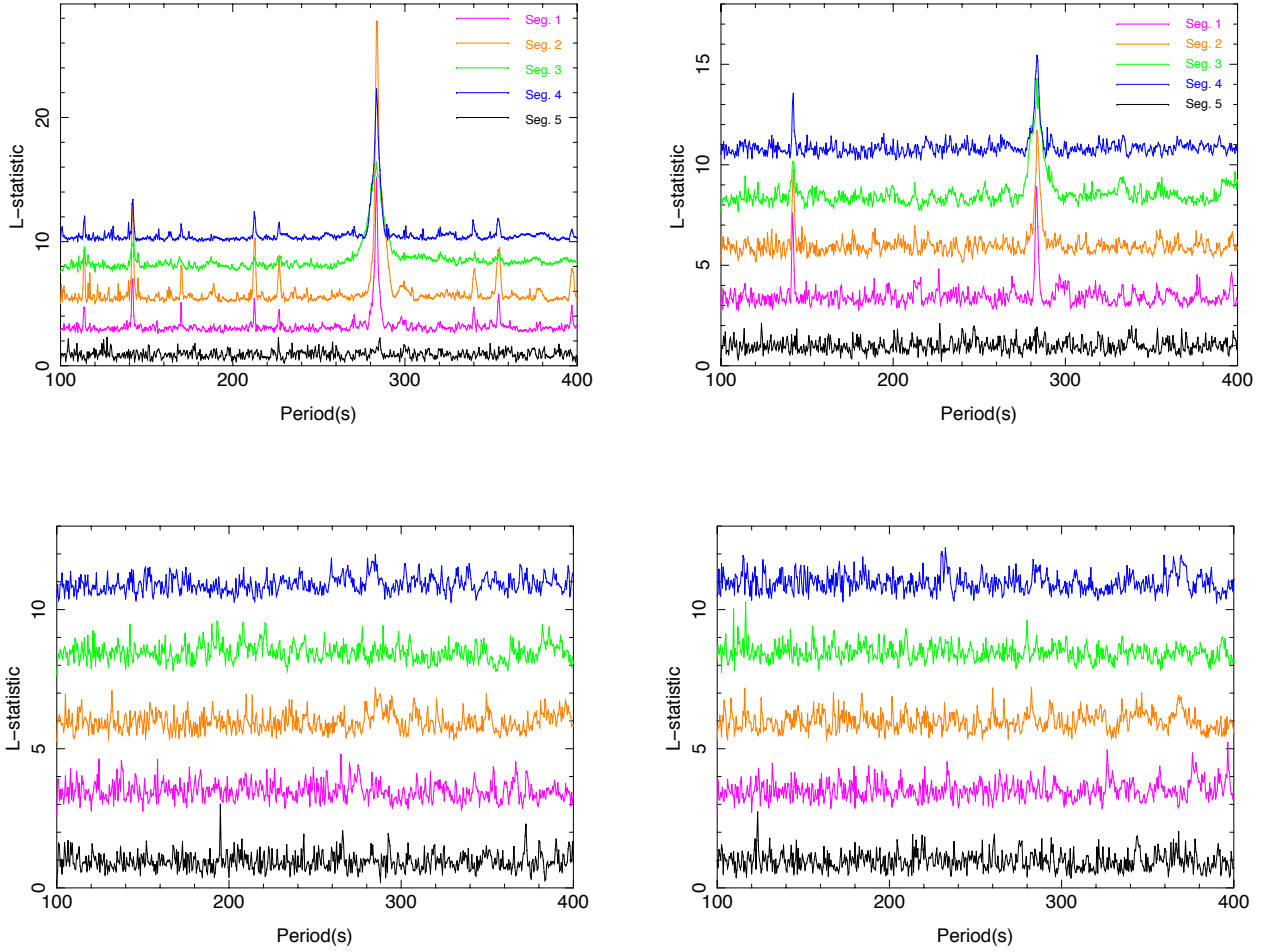


**Figure 3.** Statistical significance of the pulsation period for the continuum (3–6 keV, upper left panel; 7.5–10 keV, upper right panel), the low-energy band (1–2.1 keV, lower left panel), and the Fe K $\alpha$  line (lower right panel) during different segments. The curves of Seg. 1–4 are shifted upwards by 2.5, 5.0, 7.5, 10.0, respectively. The color scheme used in the lower panel is the same as the upper panel.

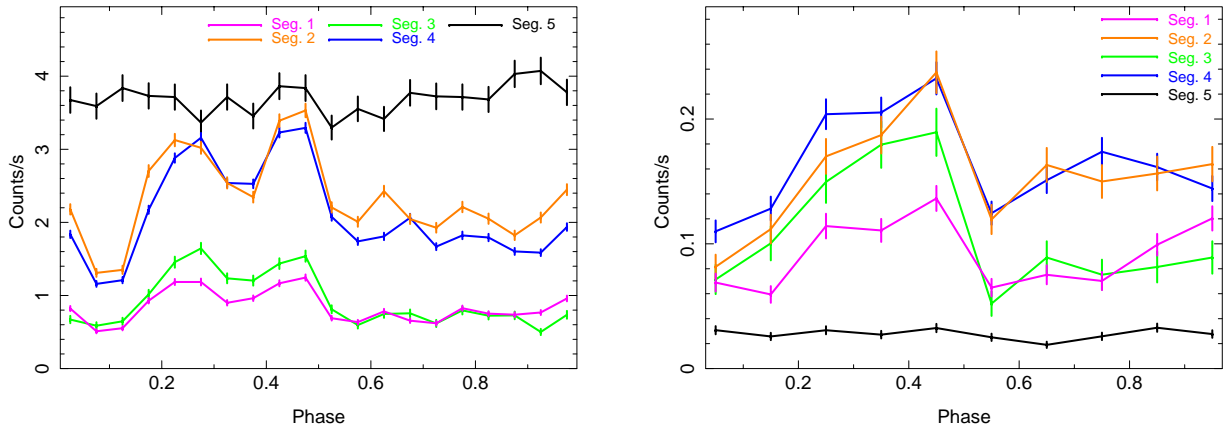


**Figure 4.** Pulse profiles of the continuum within 3–6 keV (left panel) and 7.5–10 keV (right panel) for Seg. 1 to 5. For clarity, the profile of Seg. 5 is multiplied by a factor of 12 in the left panel. Error bars indicate  $1\sigma$  uncertainty.

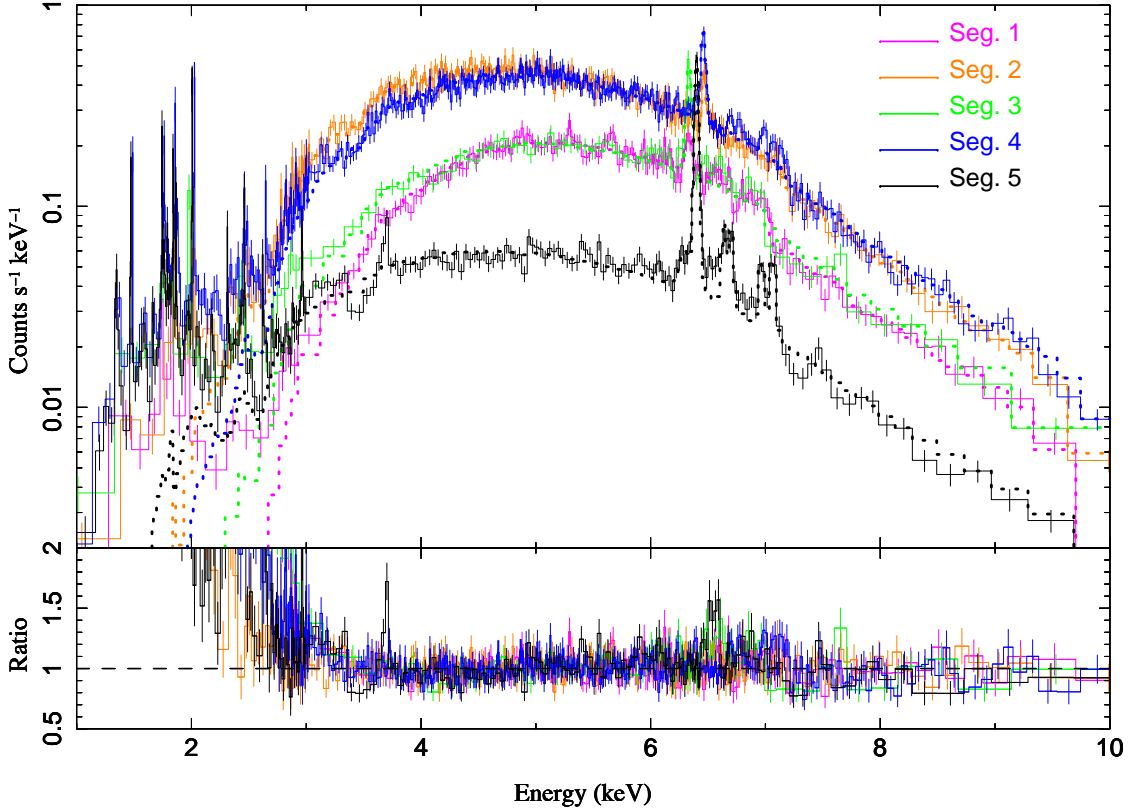


**Figure 5.** Extracted spectra of Vela X-1 for all five segments. For clarity, the spectra of Seg. 1 and Seg. 3 are redshifted by 0.01, and the spectra of Seg. 2 and Seg. 4 are blueshifted by 0.01. The histograms represent the observed data and the dotted lines represent the models fitted to the energy range of 3–10 keV.

value of neutral Fe  $K\alpha_1$  and Fe  $K\alpha_2$  (Krause & Oliver 1979). For the spectrum of Seg. 5, we add five additional Gaussian lines, representing Compton shoulder of Fe  $K\alpha$  line, Fe XXV forbidden line, Fe XXV resonance line, Fe XXVI Ly $\alpha$  line, and Fe  $K\beta$  line respectively. As shown in previous studies (e.g. Schulz et al. 2002; Watanabe et al. 2006; Grinberg et al. 2017), the low-energy spectrum of Vela X-1 is composed of many photoionized lines and neutral fluorescence lines, indicating the coexistence of the cool and hot gas around the neutron star. We limit the fitting energy range to 3–10 keV to avoid the complex low-energy lines. The fitting results are listed in Table 1 and 2 and over-plotted in Fig. 5 as dotted lines. The absorption-corrected luminosity within 2–10 keV and the Fe  $K\alpha$  EW are also listed in Table 1. Note that the fitting is only aimed to quantify the observed spectral differences, not necessarily representing the intrinsic spectral properties. This is especially true for Seg. 5, the emission of which should be dominated by scattered component.

From Table 1, we see that the continuum flux of the low state of Seg. 5 dropped by a factor of 10 compared to that of Seg. 4. On the other hand, the Fe  $K\alpha$  fluxes rise in Seg. 3 and then remain at a similar level. As a consequence, the

Fe  $K\alpha$  EW of Seg. 5 is very high,  $\sim 0.6$  keV, which is rarely seen during non-eclipse periods and is comparable to that of the eclipse period (Watanabe et al. 2006).

To further illustrate the nature of the low state of Seg. 5, in Fig. 6, we compare the eclipse spectrum (extracted from ObsID 1926, observed by *Chandra*/HETG during the eclipse phase of Vela X-1) to the spectrum of Seg. 5. The eclipse spectrum is multiplied by a factor of 17. It is interesting to see that their overall shapes are quite similar. Highly-ionized Fe XXV and Fe XXVI lines are not present in the eclipse spectrum. Below 2.5 keV, the eclipse spectrum is relatively higher than the spectrum of Seg. 5, indicating less low energy absorption of the eclipse spectrum. Flux variations of Vela X-1 due to variable absorptions with a changing column density  $\sim 5 \times 10^{22} \text{ cm}^{-2}$  have been reported previously, and they could be caused by the unsteady accretion flow (e.g. Martínez-Núñez et al. 2014; Grinberg et al. 2017). Apparently, the eclipse-like spectrum of Seg. 5 is quite different from those variations caused by column density changes  $\sim 5 \times 10^{22} \text{ cm}^{-2}$ .

**Table 1.** Fitting results of an absorbed powerlaw plus a Gaussian line ( $wabs \times powerlaw + zgauss$ ).

Seg.	Absorbed powerlaw				Fe K $\alpha$ line			Luminosity <sup>3</sup> ( $10^{35}$ erg/s)	$\chi^2_\nu$
	$N_H(10^{22} \text{ cm}^{-2})$	$\Gamma$	$N_1^1$	$\sigma$ (eV)	$N_2^2$	$z$ ( $10^{-4}$ )	$EW$ (eV)		
1	$27.5 \pm 1.3$	$1.2 \pm 0.1$	$0.22 \pm 0.06$	$21.5 \pm 10.0$	$5.7 \pm 1.7$	$9.3 \pm 15.0$	$37.0 \pm 11.0$	$11.4 \pm 1.7$	1.01
2	$14.3 \pm 0.9$	$1.3 \pm 0.1$	$0.40 \pm 0.08$	$4.2 \pm 4.0$	$9.2 \pm 2.2$	$-6.0 \pm 6.8$	$34.8 \pm 8.3$	$16.5 \pm 2.3$	0.93
3	$17.4 \pm 1.8$	$0.5 \pm 0.2$	$0.06 \pm 0.02$	$17.4 \pm 5.6$	$22.2 \pm 3.5$	$3.2 \pm 6.6$	$148.0 \pm 23.3$	$7.6 \pm 0.8$	1.49
4	$15.5 \pm 0.7$	$1.0 \pm 0.1$	$0.25 \pm 0.04$	$12.6 \pm 3.3$	$24.1 \pm 2.4$	$5.4 \pm 3.5$	$86.6 \pm 8.6$	$15.8 \pm 1.0$	1.29
5	$5.7 \pm 1.2$	$0.14 \pm 0.13$	$0.005 \pm 0.001$	$11.1 \pm 1.6$	$22.7 \pm 1.2$	$-1.1 \pm 1.6$	$588.6 \pm 31.1$	$1.59 \pm 0.1$	2.26

<sup>1</sup> Normalization of the powerlaw, in units of photons  $\text{keV}^{-1} \text{cm}^{-2} \text{s}^{-1}$  at 1 keV.

<sup>2</sup> Normalization of the Gaussian line, in units of  $10^{-4}$  photons  $\text{cm}^{-2} \text{s}^{-1}$ .

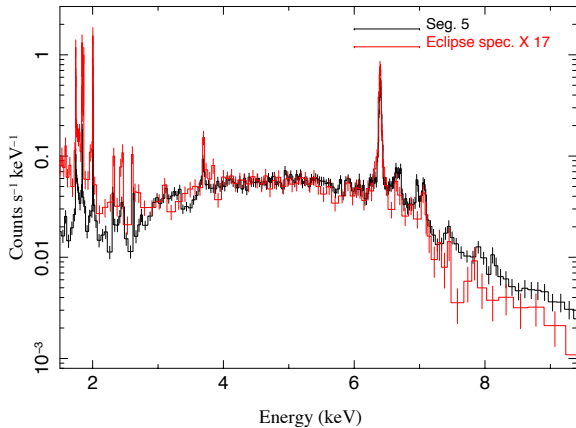
<sup>3</sup> 2–10 keV absorption-corrected luminosity.

**Table 2.** Additional Gaussian lines ( $zgauss$  model, fixing redshift to 0) fitted to the spectrum of Seg. 5.

	Fe K $\alpha$	Compton shoulder	Fe XXV F[z]	Fe XXV R[w]	Fe XXVI Ly $\alpha$	Fe K $\beta$
$N^1$	$2.2 \pm 0.7$	$3.0 \pm 0.6$	$2.9 \pm 0.6$	$2.9 \pm 0.7$	$3.5 \pm 0.8$	
$E$ (keV)	$6.29 \pm 0.02$	$6.639 \pm 0.007$	$6.701 \pm 0.007$	$6.964 \pm 0.008$	$7.064 \pm 0.007$	
$\sigma$ (eV) <sup>2</sup>	40	10	10	10	10	

<sup>1</sup> Normalization of the Gaussian line, in units of  $10^{-4}$  photons  $\text{cm}^{-2} \text{s}^{-1}$ .

<sup>2</sup> All the line widths in this table have been fixed during fitting.

**Figure 6.** Comparison of the spectrum of the extended low state of Seg. 5 (black) with the eclipse spectrum of Vela X-1 (red). The eclipse spectrum is multiplied by a factor of 17. Their overall shapes are quite similar.

## 5 DISCUSSION AND CONCLUSION

At the onset of an unusual spin-up period of Vela X-1, we have found an extended low state at orbital phases of 0.16–0.2, lasting for at least 30 ks, until the end of the observation. During this low state, the continuum pulsation is almost disappeared, and the Fe K $\alpha$  line has an eclipse-like EW of 0.6 keV. Highly-ionized Fe XXV and Fe XXVI lines are also very prominent in the low state. These highly-ionized lines were already present during the preceding flare period, but with a weaker contrast due to a stronger continuum level. The observed spectrum below 2 keV is dominated by

emission lines, which are also prominent in the low state, similar to the Fe K $\alpha$  line.

The phenomena of low states with pulsation cessation of Vela X-1 have been reported previously (e.g. Hayakawa 1984; Inoue et al. 1984; Lapshov et al. 1992; Kreykenbohm et al. 1999). The extended low state we found here is similar to that presented by Kretschmar et al. (2000). They reported a complete low state (lasting for  $\sim 15$  ks), during which the pulsation ceased, and significant non-pulsed emission remained. Thanks to the wide energy range of RXTE (2–60 keV), they found that the pulsation cessation of high energy photons (above 10 keV) was less prominent than low energy photons, and the pulsation of high energy photons recovered earlier than low energy photons. They proposed a scenario that the pulsar was temporarily obscured by a thick clump ( $N_H \sim 2 \times 10^{24} \text{ cm}^{-2}$ ), which was thought to be on a spatial scale of  $10^{13}$  cm (283 lt-s) to destroy the coherence. We note that this scale is  $\sim 3$  times the binary separation of Vela X-1, much larger than the typical clump sizes (about the Sobolev length,  $\sim 0.01 R_*$ ) found in recent wind simulations (e.g. Sundqvist et al. 2018).

Some of the observed low states of Vela X-1 (Kreykenbohm et al. 2008) were explained as results of the propeller effect (Illarionov & Sunyaev 1975). The unabsorbed continuum luminosity (2–10 keV) of the low state discovered here is  $\sim 1.6 \times 10^{35} \text{ erg s}^{-1}$ , far beyond that required by the propeller effect for Vela X-1 ( $\sim 6 \times 10^{32} \text{ erg s}^{-1}$ , Kreykenbohm et al. 2008), indicating that it can not be due to the propeller effect. The similar Fe K $\alpha$  fluxes between the low state and the preceding flare period indicate that the intrinsic radiation illuminating the Fe K $\alpha$ -emitting material during the low state should be similar to that of the preceding flare period.

The similarity of the spectral shapes of the low state and the eclipse phase (Fig. 6) points to a blocking scenario:

the intrinsic pulsed X-ray emission is blocked by a thick gas structure, and the observed X-ray emission is mainly due to scattered/reflected emission. To further discuss the blocking scenario by a thick gas structure, it is helpful to know the distance of the Fe K $\alpha$ -emitting gas ( $R_{\text{FeK}\alpha}$ ) around the neutron star. Because the observed Fe K $\alpha$  fluxes during the eclipse period reduced significantly (5–10%, Ohashi et al. 1984; Watanabe et al. 2006), the majority of the Fe K $\alpha$  fluxes should originate from a region smaller than the radius of the donor star (70 lt-s). From the observed Fe K $\alpha$  fluxes within a few hours before the egress, Ohashi et al. (1984) inferred a limit of  $R_{\text{FeK}\alpha} < 17$  lt-s.

A natural spatial scale of the Fe K $\alpha$ -emitting region is the accretion radius, within which the wind material can be accreted by the neutron star:  $R_{\text{acc}} = 2GM/v_{\text{rel}}^2$ , where  $v_{\text{rel}}$  is the relative velocity of the neutron star with respect to the wind material. The estimated masses of the neutron star of Vela X-1 range from 1.5 to 2.2 $M_{\odot}$  (e.g. Quaintrell et al. 2003; Rawls et al. 2011; Koenigsberger et al. 2012; Falanga et al. 2015). We adopt a mass of 1.8 $M_{\odot}$  with an uncertainty about 20%. Then one get  $R_{\text{acc}} \approx 10$  lt-s for  $v_{\text{rel}} \sim 400$  km s $^{-1}$  (Giménez-García et al. 2016). We looked for the time delay between the Fe K $\alpha$  line and the continuum (3–6 keV) with the cross-correlation function for light curves in Seg. 4 and found a weak peak around 5 lt-s, similar to the accretion radius calculated above.

We note that as long as the thick gas structure is quasi-axisymmetric with respect to the rotational axis of the neutron star, the illuminating radiation on the gas structure would be similar for any spin phases, and the scattered emission will show no apparent pulsation. The gas structure does not need to be as large as the light travel distance of the spin period (283 lt-s) to destroy the coherence. Since the continuum within 7.5–10 keV in the low state shows no apparent pulsation, the column density of the thick gas should be larger than 10 $^{24}$  cm $^{-2}$  to obscure 7.5–10 keV photons significantly. The high Fe K $\alpha$  EW of the low state also requires a column density of  $N_{\text{H}} \geq 10^{24}$  cm $^{-2}$  (for a thin spherical shell,  $EW \sim 0.3$  keV  $\times N_{\text{H}}/10^{24}$  cm $^{-2}$ , Kallman et al. 2004). Such a high column density is an order of magnitude greater than the average column density observed at orbital phases of 0.16–0.2 (e.g. Doroshenko et al. 2013). There are also examples of column densities  $\sim 5 \times 10^{23}$  cm $^{-2}$  around these phases (e.g. Nagase et al. 1986; Martínez-Núñez et al. 2014). If the intrinsic X-ray emission is blocked by a thick gas clump on a spatial scale of 283 lt-s, it will also block the Fe K $\alpha$  line and the low-energy photons, which is not observed. Therefore, it is most likely that a quasi-axisymmetric thick gas structure on a scale of the accretion radius blocks the intrinsic X-ray emission and produces the observed scattering-dominated X-ray emission in the low state.

As shown in Fig. 1, there is a sharp spin-down event preceding the spin-up event. The spin-down rate fitted to the spin frequencies within MJD 57740–57774 is  $(-1.5 \pm 0.8) \times 10^{-13}$  s $^{-2}$ , while the spin-up rate fitted within MJD 57807–57831 is  $(2.3 \pm 1.3) \times 10^{-13}$  s $^{-2}$ . Shakura et al. (2012) proposed a model of subsonic settling accretion, which occurs when the plasma remains hot until it meets the magnetospheric boundary. This model works at X-ray luminosities below  $4 \times 10^{36}$  erg s $^{-1}$  and predicts a positive correlation between the torque and the luminosity. The average pulsed flux of the spin-down period (MJD 57740–57774) is

$0.9 \pm 0.3$  keV cm $^{-2}$  s $^{-1}$ , similar to that of the spin-up period (MJD 57807–57831),  $1.2 \pm 0.2$  keV cm $^{-2}$  s $^{-1}$ . This is inconsistent with the prediction of the subsonic accretion model. Furthermore, the hot shell of the subsonic accretion model is optically-thin, with a Thompson optical depth  $\sim 0.03$ , corresponding to a column density of  $4.5 \times 10^{22}$  cm $^{-2}$ . Such a column density is too low to explain the low state.

Next we discuss whether a standard thin disk model can explain the measured spin-up rate of the spin-up event. As shown in numerical simulations (El Mellah et al. 2019b), the thickness of formed disk depends on the cooling efficiency. So one should keep in mind that a thin disk model may not be applicable and the angular momentum transport might be more complex. Following Bildsten et al. (1997), we assume that a thin disk deposits its angular momentum at the magnetosphere and all its angular momentum is transported to the pulsar. The spin-up torque  $N \approx \dot{M} \sqrt{GM_X r_m}$ , where  $M_X$  is the pulsar mass and the magnetosphere radius  $r_m = \xi r_A$ , is a fraction of the Alfvén radius.  $\xi$  ranges from 0.5 to 1. The accretion rate  $\dot{M} = L_X R_X / GM_X$ , where  $L_X$  is the accretion luminosity and  $R_X$  is the pulsar radius. The Alfvén radius is:

$$r_A = \left( \frac{\mu^4}{2GM_X \dot{M}^2} \right)^{\frac{1}{7}} \quad (1)$$

where  $\mu \simeq 0.5B R_X^3$  is the magnetic moment of a dipole-like magnetic field of the neutron star, with  $B$  the surface field strength. The neutron star will spin-up at a rate:

$$\dot{\nu} = \frac{N}{2\pi I} \simeq 2.2 \times 10^{-13} \text{s}^{-2} \left( \frac{L_X}{10^{36} \text{erg s}^{-1}} \right)^{\frac{6}{7}} \times \left( \frac{B}{10^{12} \text{G}} \right)^{\frac{2}{7}} \left( \frac{10 \text{km}}{R_X} \right)^{\frac{2}{7}} \left( \frac{1.4 M_{\odot}}{M_X} \right)^{\frac{10}{7}} \xi^{\frac{1}{2}}, \quad (2)$$

where  $I \simeq 0.4 M_X R_X^2$  is the pulsar’s moment of inertia. Because the spectrum of Seg. 5 is dominated by scattered emission, one can not obtain the intrinsic spectrum to infer the luminosity of Seg. 5. So we estimate the luminosity based on the fitted spectrum of Seg. 4. We obtain a luminosity of  $\sim 7.6 \times 10^{36}$  erg s $^{-1}$ , adopting a cutoff energy of 30 keV and a fold energy of 10 keV (Kreykenbohm et al. 1999). It leads to a spin-up rate of  $\dot{\nu} \approx 9.6 \times 10^{-13}$  s $^{-2}$  for  $B = 2.6 \times 10^{12}$  G,  $R_X = 10$  km,  $M_X = 1.8 M_{\odot}$ , and  $\xi = 0.7$ . The uncertainty of the estimation mainly comes from  $L_X$ ,  $M_X$ , and  $\xi$ . Assuming all these factors have an uncertainty around 30%, the estimated  $\dot{\nu}$  should be accurate within a factor of 2. Therefore, the observed spin-up rate seems to be on the same order of magnitude for a disk accretion scenario. The preceding spin-down event could be due to accretion through a retrograde disk. Detailed simulations are needed to test whether it is possible to produce a transition from a retrograde disk to a prograde disk, with both disks lasting for tens of days. We conclude that the observed continuum pulsation cessation and the high Fe K $\alpha$  EW of Seg. 5 are consistent with the existence of an accretion disk, which blocks the intrinsic X-ray emission and leads to the following spin-up event.

The required column density of  $N_{\text{H}} \geq 10^{24}$  cm $^{-2}$  and an emitting region of 5 lt-s imply an average density of 10 $^{13}$  cm $^{-3}$ . This density is  $\sim 800$  times higher than the wind density at the location of the neutron star (Sander et al. 2018), implying that the wind material should be very condensed to form a disk. The neutral-like Fe K $\alpha$  line, with

a centroid close to 6.4 keV, implies relatively cool and low-ionized gas. These results indicate that the shocked material could be cooled efficiently.

The existence of an accretion disk was also reported for other SgXBs, such as OAO 1657-415 (Jenke et al. 2012; Taani et al. 2019), GX 301-2 (Nabizadeh et al. 2019), and Cen X-3 (Tsunemi et al. 1996). These results show that disk accretion is happening, although not always, in wind-fed SgXBs. A new mass transfer mode of wind-RLOF accretion was proposed in studies of symbiotic binaries by Mohamed & Podsiadlowski (2007, 2012). El Mellah et al. (2019a) has proposed it as a possible explanation for ULXs hosting a neutron star. Our results show that disk accretion does occur in Vela X-1, but it is not a continuous process. There are other physical factors that control the formation of disk. Further studies are needed to understand what is the dominant mechanism that leads to the formation and destruction of disk accretion.

## ACKNOWLEDGEMENTS

We thank our referee for constructive comments that improved the paper. JL acknowledges the support by National Natural Science Foundation of China (NSFC, 11773035). LG acknowledges the supported by the National Program on Key Research and Development Project (2016YFA0400804), and by the NSFC (U1838114), and by the Strategic Priority Research Program of the Chinese Academy of Sciences (XDB23040100). This research used data obtained from the *Chandra* Data Archive.

## REFERENCES

Bildsten L., et al., 1997, *ApJS*, **113**, 367  
 Boynton P. E., Deeter J. E., Lamb F. K., Zylstra G., 1986, *ApJ*, **307**, 545  
 Canizares C. R., et al., 2005, *PASP*, **117**, 1144  
 Chodil G., Mark H., Rodrigues R., Seward F. D., Swift C. D., 1967, *ApJ*, **150**, 57  
 Davidson K., Ostriker J. P., 1973, *ApJ*, **179**, 585  
 Davies S. R., 1990, *MNRAS*, **244**, 93  
 Deeter J. E., Boynton P. E., Lamb F. K., Zylstra G., 1989, *ApJ*, **336**, 376  
 Doroshenko V., Santangelo A., Nakahira S., Mihara T., Sugizaki M., Matsuoka M., Nakajima M., Makishima K., 2013, *A&A*, **554**, A37  
 El Mellah I., Sundqvist J. O., Keppens R., 2019a, *A&A*, **622**, L3  
 El Mellah I., Sander A. A. C., Sundqvist J. O., Keppens R., 2019b, *A&A*, **622**, A189  
 Falanga M., Bozzo E., Lutovinov A., Bonnet-Bidaud J. M., Fetisova Y., Puls J., 2015, *A&A*, **577**, A130  
 Giménez-García A., et al., 2016, *A&A*, **591**, A26  
 Grinberg V., et al., 2017, *A&A*, **608**, A143  
 Hayakawa S., 1984, *Advances in Space Research*, **3**, 35  
 Huenemoerder D. P., et al., 2011, *AJ*, **141**, 129  
 Illarionov A. F., Sunyaev R. A., 1975, *A&A*, **39**, 185  
 Inoue H., Ogawara Y., Ohashi T., Waki I., Hayakawa S., Kunieda H., Nagase F., Tsunemi H., 1984, *PASJ*, **36**, 709  
 Jenke P. A., Wilson-Hodge C. A., 2017, in Serino M., Shidatsu M., Iwakiri W., Mihara T., eds, 7 years of MAXI: monitoring X-ray Transients. p. 137  
 Jenke P. A., Finger M. H., Wilson-Hodge C. A., Camero-Arranz A., 2012, *ApJ*, **759**, 124

Joss P. C., Rappaport S. A., 1984, *ARA&A*, **22**, 537  
 Kallman T. R., Palmeri P., Bautista M. A., Mendoza C., Krolik J. H., 2004, *ApJS*, **155**, 675  
 Karino S., Nakamura K., Taani A., 2019, *PASJ*, **71**, 58  
 Koenigsberger G., Moreno E., Harrington D. M., 2012, *A&A*, **539**, A84  
 Krause M. O., Oliver J., 1979, *Journal of Physical and Chemical Reference Data*, **8**, 329  
 Kretschmar P., et al., 1996, *A&AS*, **120**, 175  
 Kretschmar P., Kreykenbohm I., Wilms J., Staubert R., Heindl W. A., Gruber D. E., Rothschild R. E., 2000, in McConnell M. L., Ryan J. M., eds, American Institute of Physics Conference Series Vol. 510, American Institute of Physics Conference Series. pp 163–167 ([arXiv:astro-ph/9910539](https://arxiv.org/abs/astro-ph/9910539)), [doi:10.1063/1.1303195](https://doi.org/10.1063/1.1303195)  
 Kretschmar P., et al., 2019, arXiv e-prints, [p. arXiv:1905.08578](https://arxiv.org/abs/1905.08578)  
 Kreykenbohm I., Kretschmar P., Wilms J., Staubert R., Kendziorra E., Gruber D. E., Heindl W. A., Rothschild R. E., 1999, *A&A*, **341**, 141  
 Kreykenbohm I., et al., 2008, *A&A*, **492**, 511  
 Lapshov I., Sunyaev R., Chichkov M., Dremin V., Brandt S., Lund N., 1992, *Soviet Astronomy Letters*, **18**, 16  
 Leahy D. A., Darbro W., Elsner R. F., Weisskopf M. C., Sutherland P. G., Kahn S., Grindlay J. E., 1983, *ApJ*, **266**, 160  
 Martínez-Núñez S., et al., 2014, *A&A*, **563**, A70  
 Martínez-Núñez S., et al., 2017, *Space Sci. Rev.*, **212**, 59  
 McClintock J. E., et al., 1976, *ApJ*, **206**, L99  
 Mohamed S., Podsiadlowski P., 2007, in Napiwotzki R., Burleigh M. R., eds, Astronomical Society of the Pacific Conference Series Vol. 372, 15th European Workshop on White Dwarfs. p. 397  
 Mohamed S., Podsiadlowski P., 2012, *Baltic Astronomy*, **21**, 88  
 Nabizadeh A., Mönkkönen J., Tsygankov S. S., Doroshenko V., Molkov S. V., Poutanen J., 2019, *A&A*, **629**, A101  
 Nagase F., Hayakawa S., Sato N., Masai K., Inoue H., 1986, *PASJ*, **38**, 547  
 Ohashi T., et al., 1984, *PASJ*, **36**, 699  
 Quaintrell H., Norton A. J., Ash T. D. C., Roche P., Willems B., Bedding T. R., Baldry I. K., Fender R. P., 2003, *A&A*, **401**, 313  
 Raubenheimer B. C., 1990, *A&A*, **234**, 172  
 Rawls M. L., Orosz J. A., McClintock J. E., Torres M. A. P., Bailyn C. D., Buxton M. M., 2011, *ApJ*, **730**, 25  
 Sadakane K., Hirata R., Jugaku J., Kondo Y., Matsuoka M., Tanaka Y., Hammerschlag-Hensberge G., 1985, *ApJ*, **288**, 284  
 Sander A. A. C., Fürst F., Kretschmar P., Oskinova L. M., Todt H., Hainich R., Shenar T., Hamann W. R., 2018, *A&A*, **610**, A60  
 Schulz N. S., Canizares C. R., Lee J. C., Sako M., 2002, *ApJ*, **564**, L21  
 Shakura N., Postnov K., Kochetkova A., Hjalmarsdotter L., 2012, *MNRAS*, **420**, 216  
 Shapiro S. L., Lightman A. P., 1976, *ApJ*, **204**, 555  
 Sundqvist J. O., Owocki S. P., Puls J., 2018, *A&A*, **611**, A17  
 Taani A., Karino S., Song L., Al-Wardat M., Khasawneh A., Mardini M. K., 2019, *Research in Astronomy and Astrophysics*, **19**, 012  
 Tsunemi H., Kitamoto S., Tamura K., 1996, *ApJ*, **456**, 316  
 Wang Y. M., 1981, *A&A*, **102**, 36  
 Watanabe S., et al., 2006, *ApJ*, **651**, 421  
 van Kerkwijk M. H., van Paradijs J., Zuiderwijk E. J., Hammerschlag-Hensberge G., Kaper L., Sterken C., 1995, *A&A*, **303**, 483

This paper has been typeset from a  $\text{\TeX}/\text{\LaTeX}$  file prepared by the author.